frontiers | Frontiers in Earth Science

TYPE Original Research
PUBLISHED 05 January 2023
DOI 10.3389/feart.2022.994153

OPEN ACCESS

EDITED BY
Antoni Camprubí,
National Autonomous University of Mexico, Mexico

REVIEWED BY
Tingting Gu,
Purdue University, United States
Linda Pastero,
University of Turin, Italy

*CORRESPONDENCE
Jing Xu,
xujing3800@126.com

SPECIALTY SECTION
This article was submitted to Economic Geology, a section of the journal Frontiers in Earth Science

RECEIVED 14 July 2022
ACCEPTED 29 August 2022
PUBLISHED 05 January 2023

CITATION
Xu J, Ciobanu CL, Cook NJ, Slattery AD, Ehrig K, Wade BP, Courtney-Davies L and Wang L (2023), Tin-bearing magnetite with nanoscale Mg-Si defects: Evidence for the early stages of mineralization in a skarn system. *Front. Earth Sci.* 10:994153. doi: 10.3389/feart.2022.994153

Tin-bearing magnetite with nanoscale Mg-Si defects: Evidence for the early stages of mineralization in a skarn system

Jing Xu[1]*, Cristiana L. Ciobanu[2], Nigel J. Cook[3], Ashley D. Slattery[4], Kathy Ehrig[5], Benjamin P. Wade[4], Liam Courtney-Davies[6] and Liyuan Wang[1]

[1]Zijin School of Geology and Mining, Fuzhou University, Fuzhou, China, [2]School of Chemical Engineering and Advanced Materials, The University of Adelaide, Adelaide, SA, Australia, [3]School of Civil, Environmental and Mining Engineering, The University of Adelaide, Adelaide, SA, Australia, [4]Adelaide Microscopy, The University of Adelaide, Adelaide, SA, Australia, [5]BHP Olympic Dam, Adelaide, SA, Australia, [6]John de Laeter Centre, Curtin University, Perth, WA, Australia

Tin-bearing magnetite is reported from several types of magmatic-hydrothermal ore deposits. The question of whether tin is incorporated within solid solution, as Sn^{4+}, or as nanoinclusions remains open, however. We report a micron- to nanoscale investigation of Sn (Mg, Si)-bearing magnetite from serpentinite in the Dulong Zn-Sn-In skarn, South China, with the dual aims of understanding the mechanisms involved in accommodating Sn and associated elements into the Fe-oxide, and the inferences that this carries for constraining the early stages of skarn formation. Magnetite preserves a range of textures that record the evolution of metasomatism during prograde growth of grain cores and retrograde rim replacement. Observations reveal the presence of chondrodite and sellaite (MgF_2) as nanoscale inclusions preserved in magnetite. This implies initiation of the Dulong mineralizing system during a humite-bearing, magnesium skarn stage. Magnesium-Si defects, forming along (110) planes prior to Sn-enrichment, are recognized for the first time. Release of high volatile, F-rich fluids is interpreted to lead to precipitation of cassiterite inclusions along <111*> directions in magnetite.

KEYWORDS

magnetite, HAADF STEM, crystal structure, skarn, Dulong, cassiterite, humite group

1 Introduction

Magnetite is a ubiquitous mineral in a wide range of different types of ore deposit, including Fe-Cu skarns, iron oxide-copper-gold (IOCG) and iron oxide apatite (IOA) systems, banded iron formations (BIF), and magmatic Fe-Ti-V and Ni-Cu-PGE deposits. Trace element geochemistry, which is commonly used to define distinct sub-types or generations of accessory minerals (e.g., Mao et al., 2016; Kontonikas-Charos et al., 2019) is now also extensively applied to magnetite (e.g., Wang et al., 2018). Magnetite is a refractory mineral and represents an untapped record of genetic information that is

preserved as incorporated trace elements, mineral inclusions at various scales, as well as structural defects. Thus, nanoscale studies may represent a particularly valuable auxiliary tool to diagnose the earliest stage of evolving hydrothermal systems (Cook et al., 2022a). This is in agreement with the significant advantage to be gained by combining multiple techniques to adequately correlate petrographic and geochemical evidence across different scales of observation (Cook et al., 2017).

The incorporation of trace elements, including Mg, Al, Si, Ca, Ti, V, Cr, Sn and W, into magnetite, has prompted many microbeam studies focusing on fingerprinting of deposit types, thus allowing evaluation of genetic models (e.g., Neumann et al., 2017; Yin et al., 2019; Verdugo-Ihl et al., 2021). Recent nanoscale studies of magnetite from IOCG and IOA systems have used high angle annular dark field scanning transmission electron microscopy (HAADF STEM) imaging to better understand the physical nature of these trace elements. It has been shown that such elements, notably Si, are not always lattice-bound, rather, they can occur as sub-micron scale nanoparticles (Deditius et al., 2018; Ciobanu et al., 2019, 2022; Verdugo-Ihl et al., 2020; Huang and Beaudoin, 2021; Cook et al., 2022b).

The versatility of Z-contrast imaging techniques such as HAADF STEM for elucidating the relative roles of solid solution and inclusions in a host mineral is emphasized by studies of 'silician magnetite' initially defined as containing >1 wt% SiO_2 (Shiga, 1988) and first synthesized at 6–10 GPa and 1,200°C (Ohtaka et al., 1997). Silician magnetite is typified by presence of Si-Fe nanoprecipitates (γ-$Fe_{1.5}SiO_4$) as lamellae along <111*> directions of width $2d_{111}$ in host magnetite in both BIF and IOCG deposits (Xu et al., 2014; Ciobanu et al., 2019, 2022; Cook et al., 2022b). Corroborated by the presence of other silicate inclusions, silician magnetite is recognized as forming at a wide range of temperatures, spanning from ≥400°C in IOCG breccias with alkali-calcic alteration (Ciobanu et al., 2019; Verdugo-Ihl et al., 2020) to ≥600°C in granites metamorphosed at amphibolite facies (Ciobanu et al., 2022), thus well above the low-temperature depositional environment of BIFs (≤250–300°C; Huberty et al., 2012).

A comparable approach can be undertaken for Sn-bearing magnetite. Tin, exsolved as cassiterite inclusions in magnetite has been long recognized from micron-scale investigations (Desborough and Sainsbury, 1970; Wang et al., 2012; Wang et al., 2018). Although published data show that average Sn concentrations in magnetite are generally no more than a few tens of ppm (e.g., Nadoll et al., 2014), concentrations commonly reach hundreds and even thousands of ppm in relatively Sn-rich systems (e.g., Huanggang Fe-Sn skarn, China; Mei et al., 2014; Olympic Dam IOCG, Australia,Verdugo-Ihl et al., 2020). As proposed by Desborough and Sainsbury (1970), high concentrations of Sn in magnetite represents a geochemical tracer for, and pathfinder to, Sn mineralization. Synthesis experiments at 1,400°C demonstrate that magnetite can be doped with Sn^{4+} giving the nominal composition $Sn_xFe_{3-x}O_4$, where $0<x<0.6$ (Hernández-Gómez et al., 2001). Substitution mechanisms for Sn incorporation into magnetite as Sn^{4+} may be either require a vacancy (e.g., Barkov et al., 2008), or be part of a coupled substitution with other divalent elements (e.g., Chen et al., 1992; Wang et al., 2018).

Magnetite, containing inclusions of cassiterite, was reported from the Dulong Zn-Sn-In deposit, Southwest China (Xu et al., 2021a). Whereas magnetite and cassiterite are distinct components of the calcic skarn in this deposit, the presence of cassiterite inclusions is limited to serpentine-bearing rocks at the contact to marble. Such Sn-bearing magnetite resembles the cassiterite-in-magnetite reported from small bodies of tactites (rocks of complex mineralogical composition, formed by contact metamorphism and metasomatism of carbonate rocks) in fractured marble near the granite at Lost River tin Mine (Alaska; Desborough and Sainsbury, 1970). Wang et al. (2018) reported stanniferous magnetite from calcic skarn assemblages in the Haobugao Fe-Zn skarn deposit (Great Xing'an Range, China) and contended that Sn-enriched, cassiterite-bearing magnetite forms as temperature decreases. In contrast, the preferential distribution of Sn in magnetite from serpentine rocks at Dulong, but conspicuously not in the calcic skarn, prompts the question of whether such an association can instead be related to an initial skarn stage. This same stage is also characterized by the highest concentrations of indium in sphalerite from pyrrhotite-bearing hornfels (biotite schist) at the contact with marble (Xu et al., 2021b).

Tin-bearing magnetite from Dulong has been investigated down to the nanoscale to understand its origin and association with serpentine rocks. Skarn systems are the result of fluid-rock interaction between a (typically) carbonaceous protolith and hydrothermal fluids, and result in patterns of mineralogical zonation generally defined by calc-silicates such as garnet and pyroxene (e.g., Einaudi et al., 1981; Meinert, 1992; Meinert et al., 2005) but also high-temperature Mg-silicates, such as forsterite, humite, and/or chondrodite, (e.g., Cioflica et al., 1971, 1977; Gower et al., 1985; Ciobanu and Cook, 2004; Yao et al., 2014). Although not always well preserved, and indeed often not recorded at all, the occurrence of Mg-silicates is convincing evidence for an early magnesian skarn stage and may, in some cases, be associated with Au, Cu, W, Mo or B mineralization (e.g., Zhao et al., 1999; Cook and Ciobanu, 2001; Houzar et al., 2008; Marincea and Dumitraș, 2019; Huang et al., 2022). Intense retrogression (e.g., serpentinization) generally obliterates these minerals, particularly in F-rich systems (e.g., Houzar et al., 2008; Huang et al., 2022). Changes in redox conditions during the switch between prograde (diopside+andradite) and retrograde (hedenbergite+grossular) skarn stages also shows enrichment in elements such as W and Mo (Xu et al., 2016, 2019).

In this contribution, we bridge micron- and nanoscales of observation using complementary techniques to address Sn-rich magnetite from serpentinite in the Dulong skarn, South China

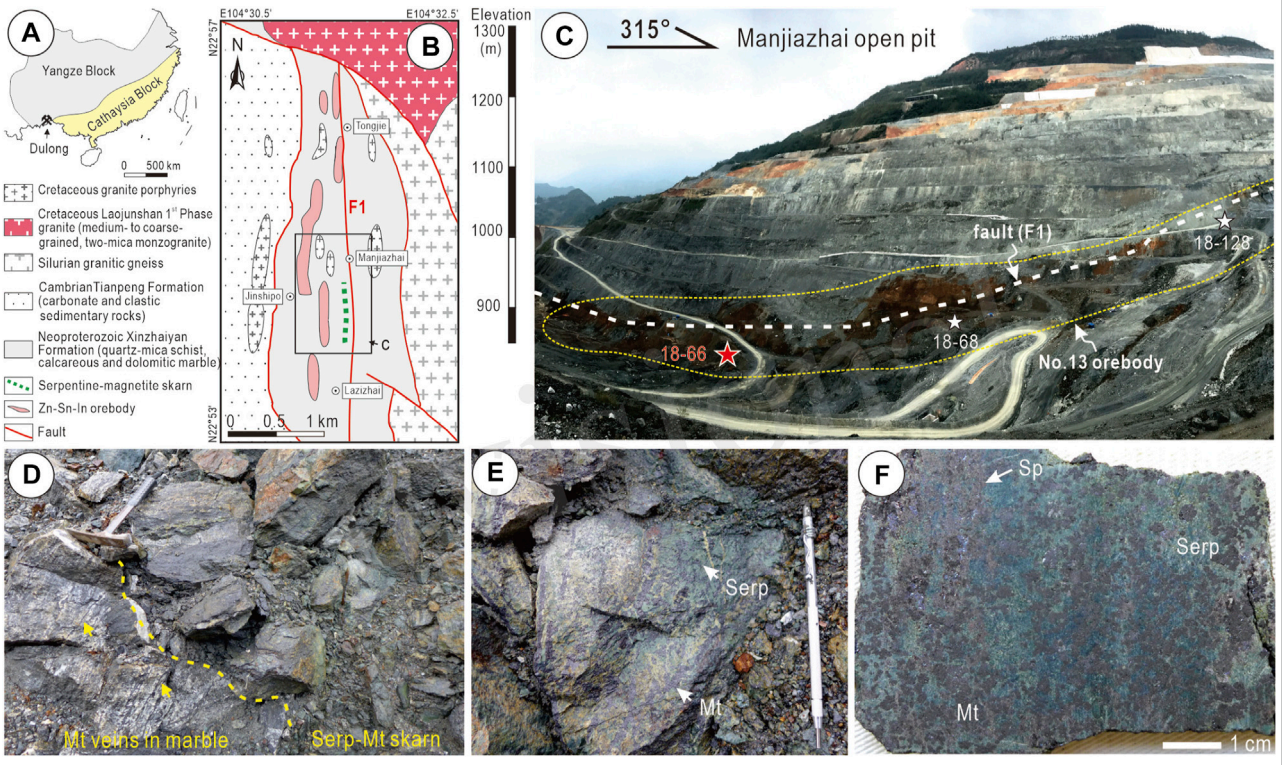

FIGURE 1
(A) Simplified structural map showing the geotectonic location of the Dulong Sn-polymetallic skarn deposit. **(B)** Geological map of the Dulong deposit after Liu et al. (2007). **(C)** Photograph showing the southern part of the Manjiazhai open pit. Red star shows the locations of serpentine-magnetite skarn studied here, and white stars show other same type of serpentine-magnetite skarn. These skarns were collected from No. 13 orebody. **(D)** The contact between serpentine (Serp)-magnetite (Mt) skarn and marble (Note yellow arrow showing the Mt veins). **(E,F)** Hand-specimen photographs showing representative Serp-Mt skarn. Brown sphalerite (Sp) can be readily recognized whereas the fine-grained cassiterite is not observable in hand specimen.

(Xu et al., 2021a; 2021b). Our objectives are to 1) characterize Sn, Mg, Si-bearing magnetite down to the atomic scale, and 2) to discuss its petrogenetic significance. We show that atypical Mg-Si defects predate and promote the Sn-enrichment in magnetite that is expressed by inclusions of cassiterite occurring alongside F- and Mg-bearing phases (chondrodite and sellaite) and serpentine. We discuss the findings in the context of an evolving skarn system.

2 Geological background

The Dulong deposit belongs to the southwestern part of the Yangtze Block (Figure 1A). A U-Pb concordia intercept age of 89.4 ± 1.4 Ma for cassiterite relates mineralization to the first phase of the Laojunshan granite (Figure 1B), which has a zircon U-Pb age of 87.5–92.9 Ma (Liu et al., 2007; Xu et al., 2015; Zhao et al., 2018). Geochemical data suggest that the Laojunshan granite is a highly fractionated S-type granite derived from partial melting of Paleoproterozoic-Mesoproterozoic pelitic basement rocks (e.g., Xu et al., 2015). The Xinzhaiyan Formation is the main host for ore and consists of interstratified quartz-mica schist, calcareous and dolomitic marble (Figure 1B). The dolomitic proportion in the marble increases with depth in the sequence (e.g., Ye et al., 2018).

The Dulong orefield contains four ore blocks (Tongjie, Manjiazhai, Jinshupo and Lazizhai) with a total contained resource of 5.0 Mt Zn, 0.4 Mt Sn, and 7 kt In (Zhao et al., 2018). Xu et al. (2021a) provided an overview of deposit zoning, skarn mineralogy and mineralization. The serpentine-magnetite skarn described here is concentrated in the relatively deep and south parts of the Manjiazhai ore block (Figures 1B,C).

Due to extensive retrogression, no prograde forsterite is observed, although previous publications (e.g., Li et al., 2018) hint at early prograde forsterite at Dulong. Xu et al. (2021a) presented data showing that, apart from cassiterite, skarn silicates (notably garnet) are important carriers of Sn. Subordinate Sn is also contained in iron-oxides and sulfides.

The LA-ICP-MS trace element concentration data for magnetite from serpentinite given by Xu et al. (2021a) show concentrations of Sn, Zn and W that are an order of magnitude

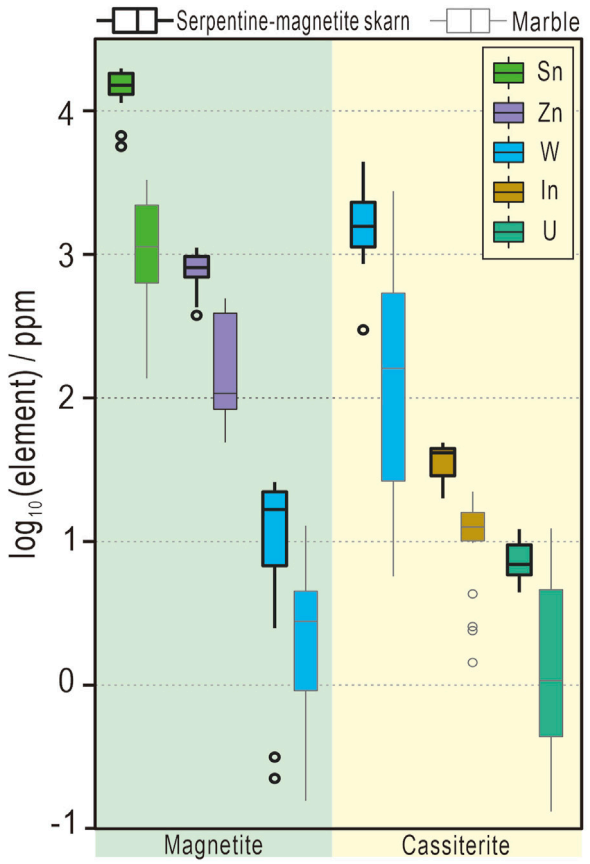

FIGURE 2
Box plot showing concentrations of selected trace elements in magnetite and cassiterite hosted within serpentine-magnetite skarn and marble, respectively. Note the distinct compositional signatures of magnetite and cassiterite in the two types of wall-rocks. Data from Xu et al. (2021a).

greater than in magnetite from marble (Figure 2). Likewise, cassiterite from serpentinite is richer in W, In and U, relative the same mineral in marble. Such differences imply formation of two distinct stages of magnetite and associated cassiterite during skarn evolution, if they can be linked to the mineralizing event rather than simply being signatures inherited from pre-existing lithologies.

3 Materials and methodology

All analytical work was carried out at Adelaide Microscopy, University of Adelaide. A Cameca SX-Five electron probe microanalyser (EPMA) was used to obtain quantitative compositional data and perform qualitative mapping of magnetite. The instrument was operated at an accelerating voltage of 15 kV and a beam current of 20 nA using a slightly defocused beam of 1 µm for quantitative analysis. Analytical conditions for mapping were adjusted to an accelerating voltage of 20 kV, a probe current of 100 nA, and dwell time of 100 ms.

HAADF STEM and energy-dispersive X-ray (EDX) mapping were performed using an ultra-high resolution, probe-corrected, FEI Titan Themis S/TEM (e.g., Ciobanu et al., 2016). FEI software was used for image acquisition (TIA v4.15), with supporting use of the drift-corrected frame integration package (DCFI) included in the Velox (v2.13.0.1138) software. Various filters (Radial Wiener, High-pass, Average and Gaussian blur) were used to eliminate noise and/or enhance images. All EDS data acquisition and processing was carried out using Velox software.

HR STEM imaging of beam-sensitive minerals was achieved using the integrated differential phase contrast (iDPC) technique, described by Lazić et al., 2016. For thin, non-magnetic samples the iDPC technique images the scalar electrostatic potential field, yielding images of the atomic species with contrast roughly proportional to the atomic number (Z). In contrast to HAADF STEM, the detectability of light elements is significantly improved. The iDPC signal is also superior to the HAADF signal, due to the use of the intense signal in the bright field disc and the noise-suppressing nature of the integration process. As a result, the iDPC imaging technique is ideal for imaging beam-sensitive materials.

Indexing of diffraction patterns was conducted with WinWulff© (v1.6) (JCrystalSoft). CrystalMaker® (v10.5.7) was used to generate crystal structure models; image simulations were created using STEM for xHREMTM (v4.1) software.

4 Results

Magnetite from serpentinite displays a broad range of intra-grain textures that correlate with measured Sn concentrations (Figure 3). Magnetite featuring Sn-rich cores (Figures 3A,B) is associated with In-bearing sphalerite (Xu et al., 2021b). These cores can be very small, resorbed, and often overgrown by asymmetric margins (Figure 3C), or display a patchiness or mottling expressed by submicron-scale inclusions of cassiterite (Figures 3D,E). Different spatial arrangements of the inclusions define an intertwined lamellar substructure in the patchy cores, as well as inclusion-free subdomains in the mottled cores (Figures 3F,G).

A representative Sn-bearing magnetite grain from serpentinite sample DL66 featuring patchy core zonation was assessed by EPMA spot analysis and element mapping at the micron scale (Table 1, Figure 4). A profile across the inclusion-free rim (Figure 4B) shows concentrations of MgO, SiO_2 and SnO_2 (up to several wt% close to the core boundary) that correlate antithetically with FeO*. The patchy texture within the core is reproduced on the Sn map, whereas the rim is marked by a band of relatively higher Mg and Si, and scattered Si-Mg-bearing inclusions (Figure 4C).

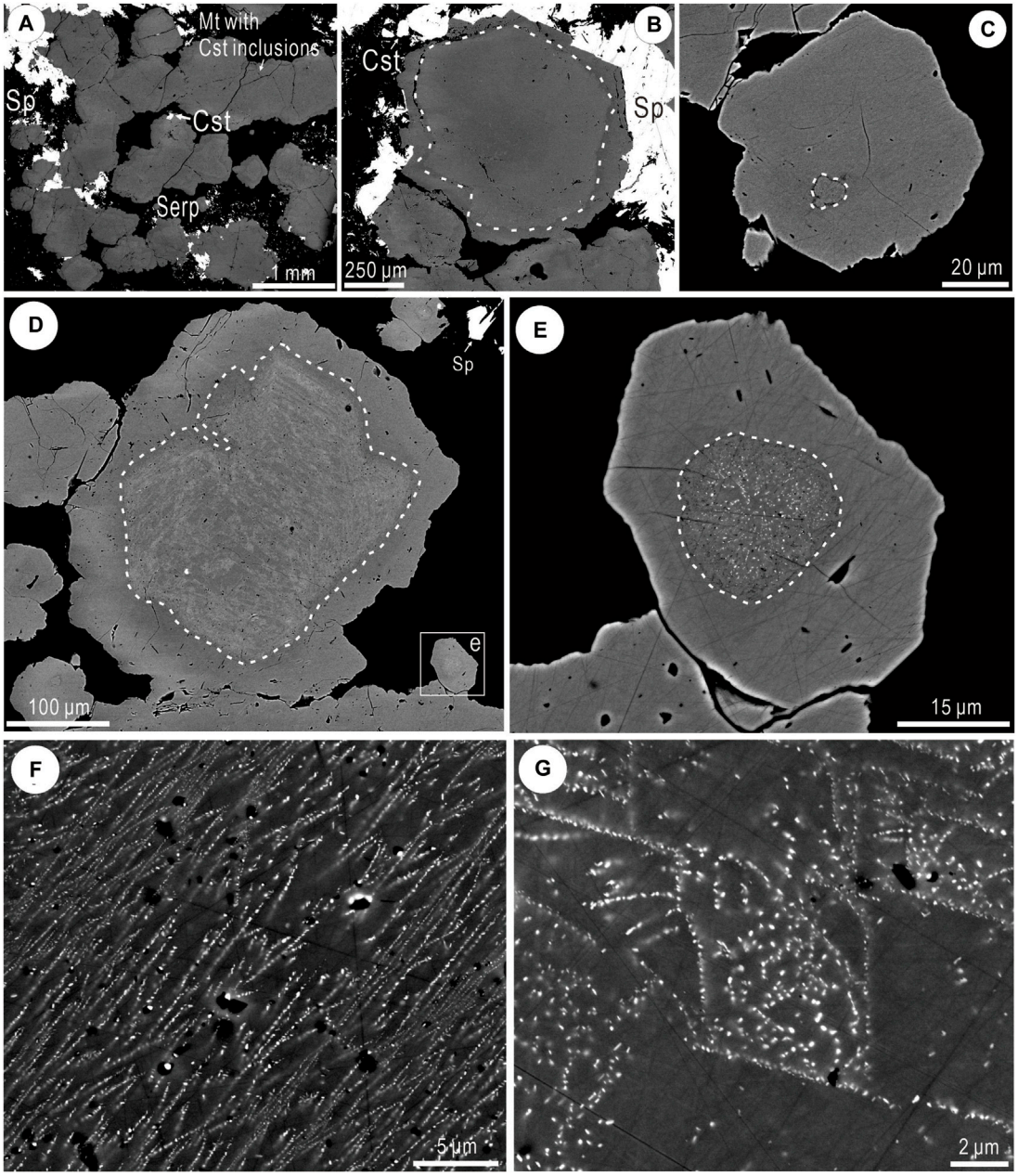

FIGURE 3
BSE images showing the appearance of magnetite (Mt) with inclusions of cassiterite (Cst). **(A)** Subhedral Mt containing Cst inclusions surrounded by sphalerite (Sp), serpentine (Serp), and coarser grained Cst. **(B)** Mt with Cst inclusions showing narrow margin without Cst inclusions. **(C)** Concentration of Cst inclusions within the small, irregular grain core. **(D)** Larger Cst-bearing core in Mt showing irregular boundary between core and rim. **(E)** Cst inclusions in core of Mt. **(F)** Crystallographically oriented Cst inclusions. **(G)** Domains of Sn-free Mt and relative coarsening of Cst inclusions.

4.1 Nanoscale characterization

The nanoscale study was conducted on a FIB-prepared TEM foil (Figure 5A) extracted from across the core-rim boundary within this grain (Figure 4C). Low-resolution HAADF STEM imaging and STEM EDS mapping of the foil (Figure 5B) reveal cassiterite particles that increase in density away from the boundary, as well as a smaller population of darker, often acicular Mg-bearing silicate inclusions with contrasting density trend relative to the same boundary. Based on composition, some of these silicate inclusions are attributable to varieties of serpentine, albeit undifferentiated.

TABLE 1 Compositional data by EPMA (wt%) for Dulong magnetite.

	40–1	40–2	40–3	40–4	40–5	40–6	40–7	40–8	40–9	40–10	40–11	40–12	40–13	40–14	40–15
CaO	<mdl	<mdl	<mdl	0.02	<mdl	<mdl	<mdl	<mdl	<mdl	<mdl	<mdl	<mdl	<mdl	<mdl	0.02
MgO	2.77	2.22	1.60	1.39	1.24	1.12	0.88	0.75	0.74	0.62	0.53	0.48	0.49	0.41	0.26
TiO_2	<mdl	<mdl	<mdl	<mdl	<mdl	<mdl	<mdl	<mdl	0.03	<mdl	<mdl	<mdl	<mdl	<mdl	<mdl
SiO_2	1.80	1.88	1.44	1.47	1.39	1.31	0.86	0.54	0.75	0.66	0.40	0.39	0.58	0.61	0.35
Al_2O_3	<mdl	<mdl	<mdl	<mdl	0.04	<mdl	<mdl	<mdl	<mdl	<mdl	<mdl	<mdl	<mdl	<mdl	<mdl
FeO	29.80	30.49	30.44	30.39	30.76	30.83	30.37	30.19	30.55	30.73	30.32	30.19	30.74	30.53	30.51
Fe_2O_3	64.90	64.17	66.41	65.64	65.84	66.07	66.57	67.43	66.95	67.32	67.47	67.11	67.34	66.20	67.18
MnO	0.10	0.09	0.08	0.12	0.07	0.09	0.08	0.09	0.09	0.07	0.06	0.07	0.08	0.00	0.06
ZnO	<mdl	0.06	0.07	0.11	<mdl	<mdl	<mdl	<mdl	<mdl	<mdl	<mdl	<mdl	<mdl	<mdl	<mdl
SnO_2	1.40	1.31	0.11	0.06	0.08	0.07	<mdl	<mdl	<mdl	0.04	0.03	<mdl	<mdl	<mdl	<mdl
SUM	100.78	100.22	100.16	99.19	99.42	99.48	98.76	98.99	99.10	99.43	98.81	98.23	99.23	97.75	98.37
No. of ions based on 32 apfu O															
Mg	1.236	0.998	0.722	0.633	0.565	0.510	0.403	0.347	0.340	0.283	0.246	0.224	0.226	0.190	0.123
Ca				0.007											0.007
Mn	0.024	0.024	0.021	0.030	0.018	0.023	0.021	0.024	0.023	0.018	0.016	0.018	0.020		0.016
Fe^{2+}	7.445	7.687	7.692	7.761	7.850	7.874	7.841	7.795	7.874	7.906	7.864	7.880	7.934	8.002	7.964
Zn		0.013	0.015	0.025											
$\sum M^{2+}$	8.705	8.723	8.450	8.457	8.433	8.407	8.266	8.166	8.237	8.207	8.127	8.121	8.180	8.193	8.110
Al					0.015										
Fe^{3+}	14.591	14.555	15.100	15.085	15.118	15.185	15.468	15.668	15.527	15.585	15.747	15.759	15.640	15.615	15.781
$\sum M^{3+}$	14.591	14.555	15.100	15.085	15.134	15.185	15.468	15.668	15.527	15.585	15.747	15.759	15.640	15.615	15.781
Si	0.538	0.565	0.436	0.450	0.424	0.399	0.266	0.166	0.231	0.202	0.123	0.121	0.180	0.193	0.110
Ti									0.006						
Sn	0.167	0.157	0.014	0.007	0.010	0.008				0.005	0.004				
$\sum M^{4+}$	0.705	0.723	0.450	0.457	0.433	0.407	0.266	0.166	0.237	0.207	0.127	0.121	0.180	0.193	0.110
SUM	24.000	24.000	24.000	24.000	24.000	24.000	24.000	24.000	24.000	24.000	24.000	24.000	24.000	24.000	24.000
FeTot	22.035	22.242	22.792	22.847	22.968	23.060	23.309	23.463	23.401	23.491	23.611	23.638	23.574	23.617	23.745
Sum-Si	23.462	23.435	23.564	23.550	23.576	23.601	23.734	23.834	23.769	23.798	23.877	23.879	23.820	23.807	23.890

Note: <mdl, below to minimum detection limit

4.1.1 Inclusions in magnetite

Cassiterite, the most abundant included phase, varies in size from nanoparticles (<100 nm in diameter; NP) to fine particles (100–2,500 nm) and with variable distribution throughout the magnetite. Many such cassiterite inclusions form binary associations with a Mg-silicate as seen from higher magnification images and element maps (Figure 6A). Although the silicate is typically far smaller than the cassiterite, their mutual boundaries suggest co-crystallization (Figure 6B). STEM EDS element maps show measurable amounts of other elements in the cassiterite, including Ti and W (as shown on the element maps), but also U and Pb. EDS STEM integrated spectra yield the empirical formula $(Sn_{0.997}Ti_{0.006}W_{0.005}Pb_{0.007}U_{0.006})_{1.021}O_2$ for cassiterite (Table 2); inclusions with acicular habit (Figure 6A) are the richest in trace elements. High-resolution images of cassiterite viewed on two main zone axes (Figures 7A–D) show a very good fit with the crystal models and with STEM simulations (Figures 7E,F). We note that cassiterite displays epitaxial relationships with magnetite, in which $<110^*>_{cassiterite}$ is parallel to $<111^*>_{magnetite}$, indicating preferential growth of Sn-bearing inclusions in the host Fe-oxide.

Fluorine was noted in other two Mg-bearing inclusions with a granular habit (Table 2, Figures 8, 9). These correspond to the Mg-fluoride sellaite (MgF_2), and a coexisting silicate distinct from serpentine. Calculated compositions for the silicate from STEM EDS data yielded the empirical formula $(Mg_{5.45}Fe_{0.26})_{5.71}(Si_{2.14}O_4)_2F_{1.16}$, indicating a species belonging to the humite family (Gibbs et al., 1970; Ottolini et al., 2000; Friedrich et al., 2001) with a best match to chondrodite, ideally $(Mg, Fe)_5(SiO_4)_2F_2$. The cation excess and F deficit can be attributed, in part, to difficulties in accurate measurement of F concentrations due to matrix effects in humite-group minerals as discussed for several analytical techniques, including EPMA (Ottolini et al., 2000).

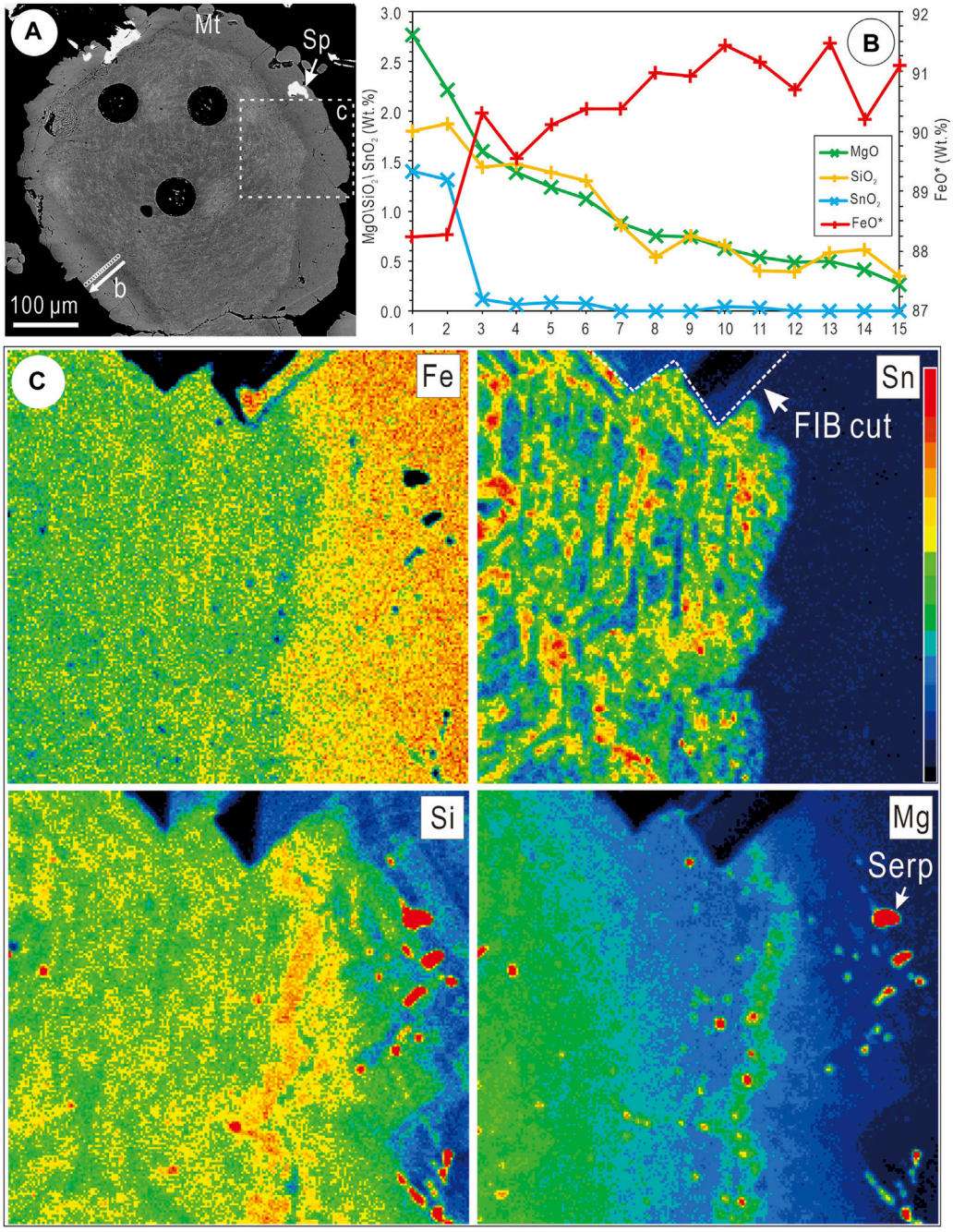

FIGURE 4
(A) BSE image showing cassiterite (Cst)-bearing magnetite (Mt) with narrow margin free of Cst partially replaced by sphalerite (Sp). Line plot in b and element maps in c are located. Black circles are LA–ICP–MS ablation craters. **(B)** Plot of EPMA data illustrating compositional change in Mg, Si, Sn, and Fe from Cst-bearing to Cst-free Mt in the outer rim. **(C)** EPMA element maps of magnetite for elements of interest (Fe, Sn, Mg and Si). Note location of FIB cut marked on **(C)**.

The chondrodite grain analyzed by STEM EDS (maps in Figure 8A, data in Table 2) was suitable for imaging only if low-dose HAADF and iDPC STEM techniques were used (Figures 8B,C). The chondrodite structure displays two different motifs when imaged on the [110] zone axis, with a relatively good correlation between the two types of images. The HAADF image (Figure 8B) shows better the motif that occurs as bright, waving strips of atoms with ~7.5 Å periodicity along the *c* axis. The iDPC

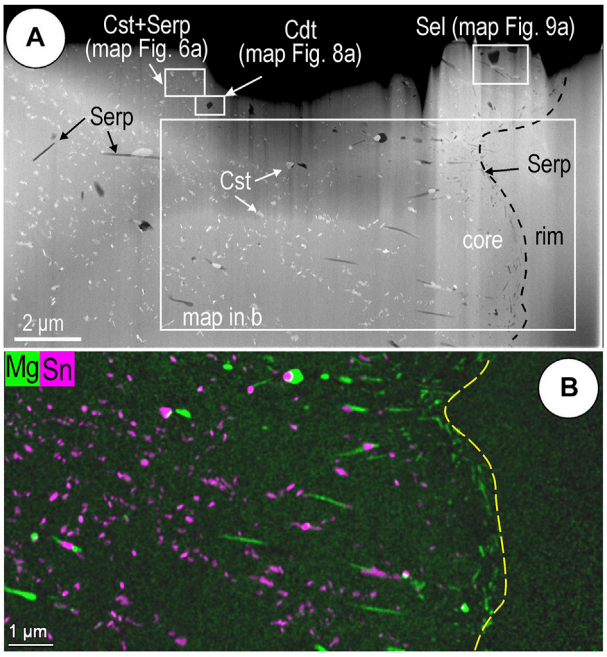

FIGURE 5
(A) Overview of studied S/TEM foil showing the contact between rim and core in magnetite. **(B)** Low-resolution STEM EDS element map showing distribution of cassiterite inclusions (Cst) that increase in density away from the grain boundary and smaller acicular serpentine (Serp) inclusions, concentrated in the boundary domain. The other Mg-, F-bearing phases, chondrodite (Cdt) and sellaite (Sel), are marked within mapped areas.

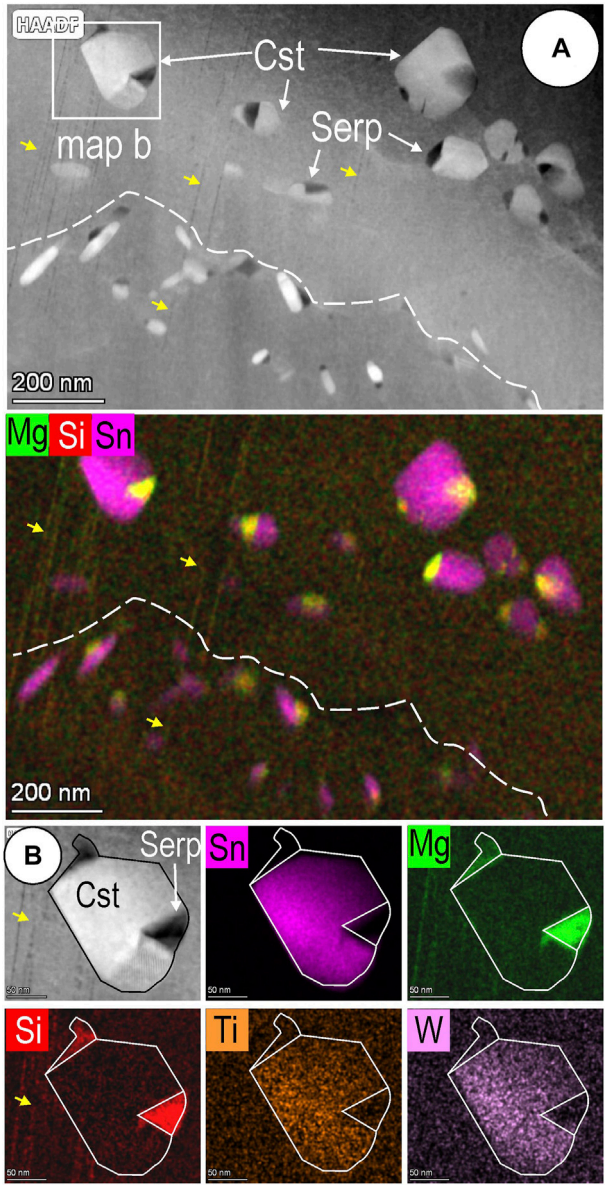

FIGURE 6
(A) HAADF STEM image and element map showing binary cassiterite (Cst)—serpentine (Serp) nanoinclusions in magnetite. Dashed line shows domain boundary between larger and smaller, acicular cassiterite inclusions. **(B)**. Detail of a single NP with mutual boundaries between phases suggestive of co-crystallization. Yellow arrows show Mg-Si-defects in magnetite crosscut by the inclusions.

image (Figure 8C), in contrast, shows a lighter, squarish, motif placed between the brighter strips. STEM simulation shows that the lighter motif on the iDPC image is attributable to the SiO_2 tetrahedra, flanked by Mg (Fe) and F cations (Figure 8D). The waving strips can be related to the overlapping Mg and F cations at the corners of the SiO_2 tetrahedra. Although the match between the images and models is imperfect, the fast Fourier transform (FFT) pattern and electron diffraction simulation (Figures 8B,D) are in excellent agreement with the identification of this mineral from the chemical composition (Table 2).

Likewise, the identification of sellaite, the second F-bearing species, was made using STEM EDS analysis and high-resolution imaging of the stubby grains preserved in the upper part of the foil (Figure 9). Calculated compositions from integrated spectra give the empirical formula $(Mg_{0.98}Fe_{0.02})F_{1.91}$ (Table 2). Element mapping (Figure 9A) shows variable content of F and Mg, mostly due to variation in the thickness and exposure of grains rather than the co-existence of different species. As in the case of chondrodite, we note that the sellaite grains are separated from the cassiterite and serpentine inclusions. Identification of sellaite is confirmed by high-resolution iDPC imaging on [100], matching the crystal structure model and STEM simulation on this plane of view (Figures 9B–E).

4.1.2 Mg-Si-bearing defects in magnetite

One of the most outstanding nanoscale features in the studied magnetite is the presence of dense fields of parallel, linear defects throughout the Sn-bearing, inclusion-rich domains, and to a lesser extent, within the margin of the foil (Figure 10). Such defects are clearly crosscut by needles of

10.3389/feart.2022.994153

TABLE 2 Compositional calculated from STEM EDS data on mapped grains.

cassiterite					**average**
Wt%	1	2	3	4 (acicular)	***n* = 4**
SnO_2	98.48	97.24	97.38	94.20	**96.82**
TiO_2	0.07	0.39	0.26	0.46	**0.30**
WO_3	0.08	0.38	0.77	1.82	**0.76**
PbO	0.99	0.90	0.89	1.31	**1.02**
UO_2	0.38	1.08	0.70	2.21	**1.09**
Total	100	100	100	100	**100**
a.p.f.u. O = 2					
Sn	0.992	0.980	0.981	0.956	**0.977**
Ti	0.001	0.008	0.005	0.009	**0.006**
W	0.001	0.002	0.005	0.012	**0.005**
Pb	0.007	0.006	0.006	0.009	**0.007**
U	0.002	0.006	0.004	0.012	**0.006**
Σ cations	1	1	1	1	**1**
chondrodite					**average**
Wt. %	1	2	3	4	***n* = 4**
SiO_2	33.88	34.52	33.71	30.23	**33.09**
FeO	2.13	2.24	2.00	12.78	**4.79**
MgO	58.25	57.48	57.23	52.90	**56.46**
F	5.74	5.75	7.06	4.09	**5.66**
TOTAL	99.35	99.35	99.35	99.35	**99.35**
O = F, Cl	2.42	2.42	2.97	1.72	**2.38**
TOTAL	96.94	96.93	96.38	97.63	**96.97**
a.p.f.u. calculated for O = 10					
Si	2.17	2.20	2.18	2.02	**2.14**
Fe(ii)	0.11	0.12	0.11	0.71	**0.26**
Mg	5.55	5.47	5.53	5.26	**5.45**
F	1.16	1.16	1.45	0.86	**1.16**
Σ cations	7.83	7.80	7.82	7.98	**7.86**
sellaite				**average**	
Wt. %	1	2	3	***n* = 3**	
FeO	0.53	0.70	3.41	**1.55**	
MgO	52.81	49.09	52.63	**51.51**	
F	46.66	50.21	43.97	**46.94**	
TOTAL	99.35	99.35	99.35	**99.35**	
a.p.f.u					
Fe(ii)	0.01	0.01	0.04	**0.02**	
Mg	0.99	0.99	0.96	**0.98**	
F	1.86	2.15	1.71	**1.91**	
Σ cations	1	1	1	**1**	

serpentine attached to grains of cassiterite (Figure 10A). In closer detail, the linear defects observed on HAADF images consist of either: 1) arrays of hexagonal-shaped nanoparticles (~5 nm in width) that appear darker than magnetite; or 2) thin, still darker lines (Figure 10B). Defect-free nanodomains are surrounded by cassiterite and serpentine inclusions (Figure 10C), and magnetite from the cassiterite-free margin of the foil is densely populated by serpentine inclusions (Figure 10D). The two types of defects are best displayed on that $[1\bar{1}0]$ zone axis in magnetite and may, or may not, overlap with one another (Figure 10E). Fast Fourier

10.3389/feart.2022.994153

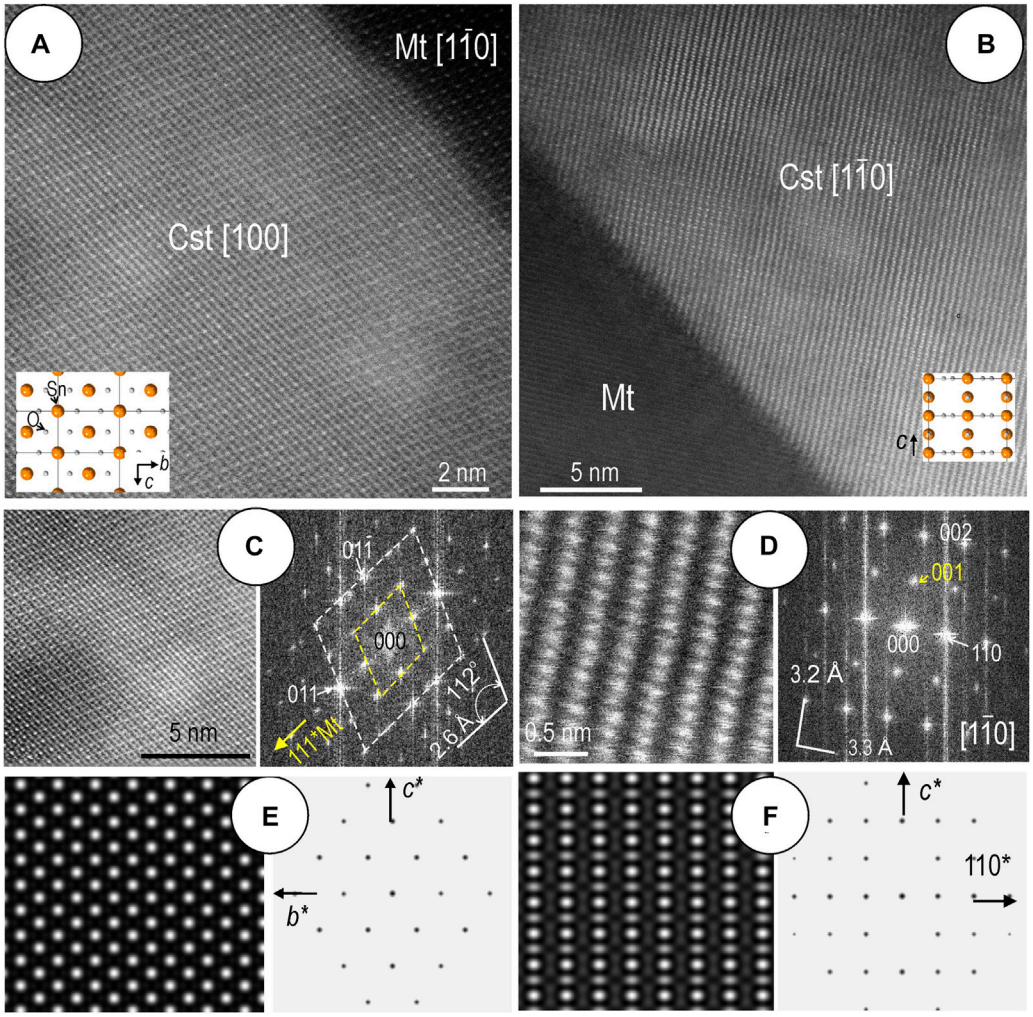

FIGURE 7
(A,B) High-resolution HAADF STEM images of cassiterite (Cst) on two main zone axes as marked. Overlays of atom fill models showing Sn and O atom columns. Note contact with magnetite (Mt) showing epitaxial orientation with cassiterite in **(A)**. **(C,D)** Image crops and fast Fourier transform (FFT) patterns for cassiterite in **(A,B)**. The FFT in **(B)** shows both cassiterite (white) and magnetite (yellow) patterns with $111^*_{Mt}\backslash\backslash 011^*_{Cst}$, and d_{111Mt} (4.8 Å) ~ $2d_{011Cst}$ (2.6 Å). **(E,F)** STEM simulations and electron diffraction patterns of cassiterite on the same zone axes showing excellent fit with the data in **a-d**.

transform patterns obtained from such areas show disorder along <110*> directions (Figure 10F). In contrast, FFT patterns obtained from areas with the hexagonal-shaped darker NPs show no modifications from ideal magnetite (Figures 10G,H). Loop-shaped defects and hexagonal to rounded, ~25 nm-diameter inclusions of serpentine located along the core-rim boundary in magnetite (Figures 10I,J) resemble the defects within the Sn-rich part of the same grain, but the smallest serpentine inclusions are five times larger than those forming parallel arrays along <110*> directions in magnetite (Figures 10E,J). Although the serpentine is not sufficiently stable under the electron beam to allow high-resolution imaging, FFT patterns indicate that it is a monoclinic variety of antigorite (Figure 10K; Dodony et al., 2002; Capitani and Mellini, 2004).

Higher magnification STEM EDS maps of areas with <110*> defects within magnetite show the presence of Si and Mg (Figure 11). The same two elements are measurable along both the lines and the hexagonal-shaped blebs (Figures 11A,C). Profiles across a set of such linear defects indicate a positive correlation between Si and Mg (Figure 11D). An antithetic distribution between Si and Mg with Fe is shown on element maps for a single line defect (Figure 12A).

High-resolution imaging shows changes in intensity and typical arrangement of atoms on [1$\bar{1}$0] magnetite (Figures 12B–D). Interpretation of the HAADF STEM images illustrating this type of defect is made considering the atom-fill crystal structure model for Fe atoms in [1$\bar{1}$0] $_{\text{magnetite}}$

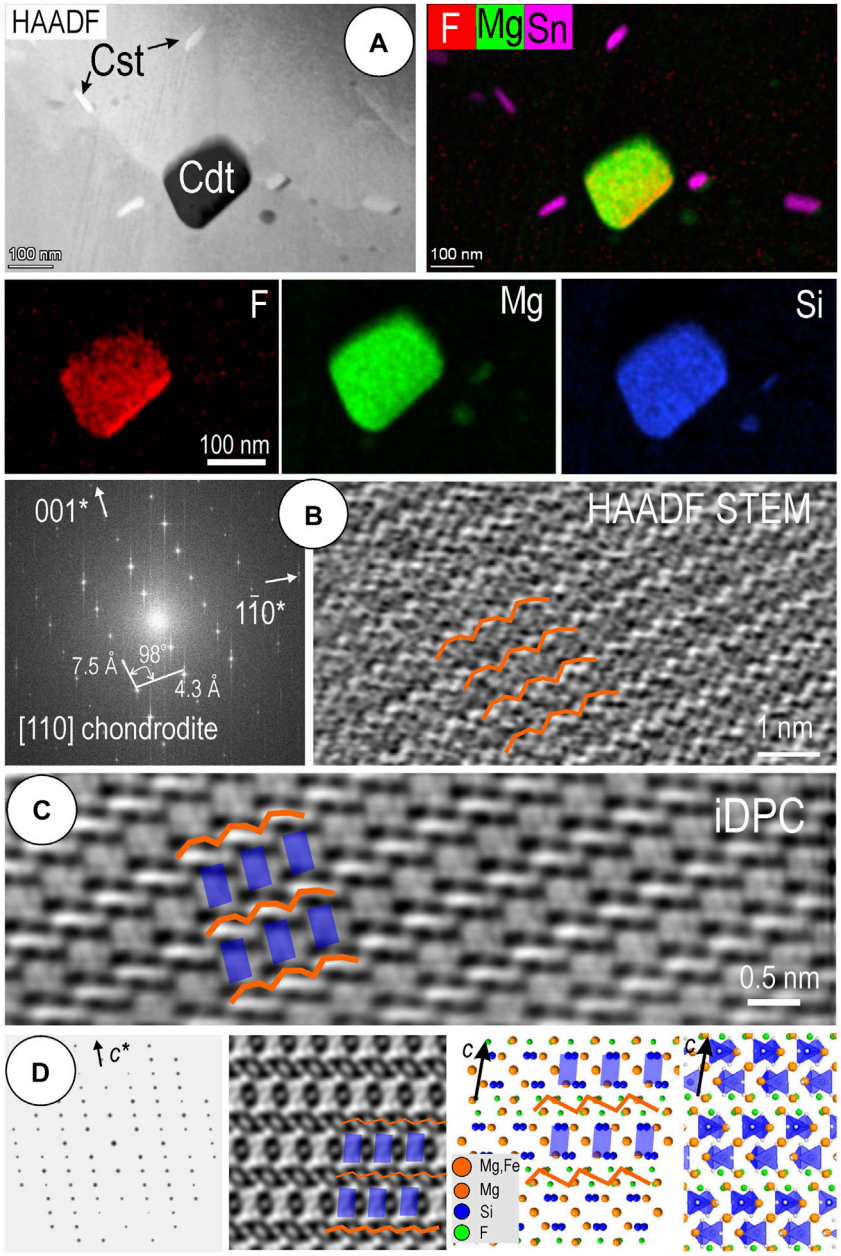

FIGURE 8
(A) HAADF image and STEM EDS maps for chondrodite (Cdt) in magnetite that contains acicular nanoinclusions of cassiterite (Cst). **(B)** FFT pattern and HAADF STEM image of chondrodite oriented as marked in square brackets for the inclusion in **(A)**. Overlays show the bright motif that occurs as bright, waving strips of atoms with ~7.5 Å periodicity along the *c* axis. **(C)** iDPC image of chondrodite showing a lighter, squarish, motif placed between the brighter strips. **(D)** Simulations of electron diffraction pattern, STEM image, atom-fill, and polyhedral models for chondrodite on the same zone axis as imaged in **(B)** and **(C)**. The STEM simulation shows that the lighter motif on the iDPC image is attributable to the SiO_2 tetrahedra, flanked by Mg (Fe) and F cations (as marked by overlays on the image and models).

(Figure 12B). The two structural sites for Fe, octahedral (M) and tetrahedral (T), form three distinct arrays along (110) planes, for simplicity marked by the numeric sequence: 3212/3212. . ., whereby the octahedral site is present either as single or double 2 M atomic columns. The 2 M sites forms a rhombic motif of brightest dots on the HAADF STEM images, each surrounded by a 10-atom ring of smaller dots, representing the M and T sites. The atom fill structure is well reproduced on STEM simulations (Figure 12B; Ciobanu et al., 2019). The overall decrease in signal intensity across the Si-Mg-bearing

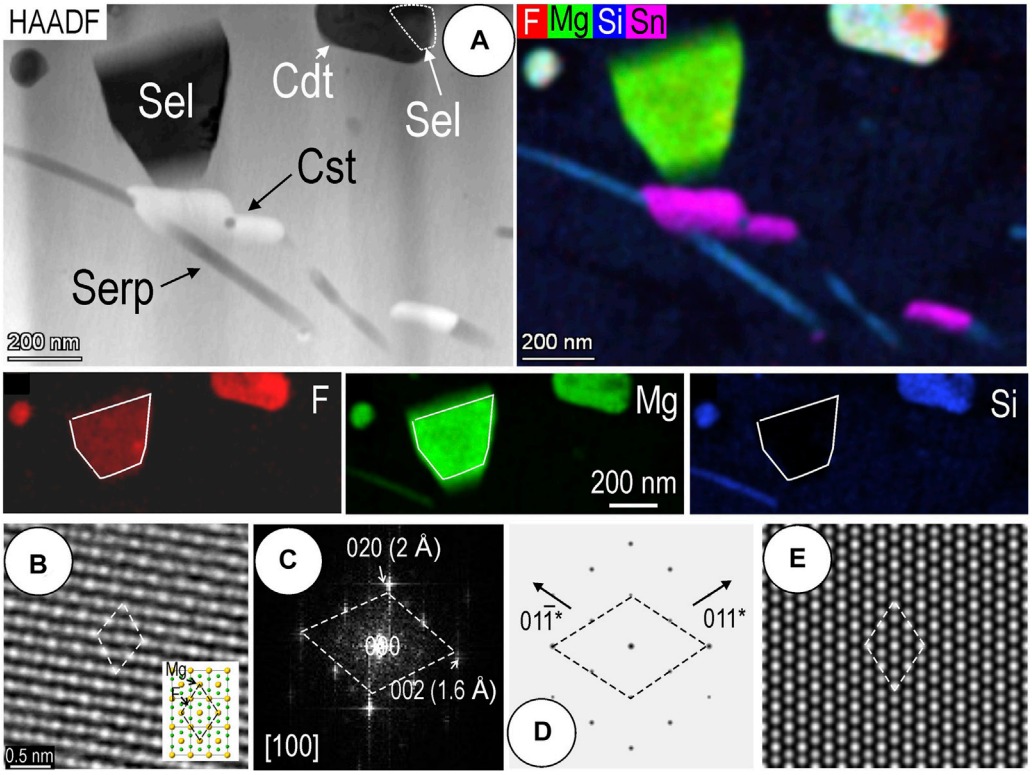

FIGURE 9
(A) HAADF image and STEM EDS maps for sellaite (Sel) in magnetite that contains acicular nanoinclusions of cassiterite (Cst), serpentine (Serp) and chondrodite (Cd). **(B,C)** iDPC image and FFT pattern for the sellaite on [100] zone axis. Overlay shows atom fill model. **(D,E)** Simulations of electron diffraction pattern and STEM image for sellaite on the same zone axis as **(B)** and **(C)**. Note good correlation with the iDPC image.

defect of ~6 Å width, representing $2d_{110}$ in magnetite, can be attributed to partial or total replacement of Fe by Mg and Si (Figure 12C). Using the same atomic model, the atomic arrangement across the defect is represented by the sequence: 3/2123/23′2/3212/3, whereby 3′ is a 3-type array with ½ (110) gaps in 2 M atoms (vacancies?) (Figure 12D). The same sequence can also be considered as produced by twinning along the 3-type arrays with ½(110) shifts. Analogous to this are the (110) twins along the 2-type arrays, leading to the sequence 2,123/2/3212/, without chemical changes, which have been reported from silician magnetite at Olympic Dam, South Australia (Cook et al., 2022b).

5 Discussion

5.1 Magnetite records early-stage mineralization–cassiterite associated with formation of humite skarn

The core-rim zonation patterns in magnetite (Figures 3, 4) could have formed during a single growth episode if we consider the micron-scale zonation patterns showing correlations between Sn, Mg, and Si with trends showing a gradual decrease from grain core to rim (Figure 4).

The magnetite grain core studied here shows up to 1.4 wt% SnO_2 (Table 1) which is within the same range (1-2 wt% Sn) that we have measured in other grains from serpentinite at Dulong (Figure 2). Although a little lower, these values are still within the same order of magnitude of Sn concentration (up to 2.82 wt% for 'magnetite 2') as those reported for low-temperature, Si-bearing magnetite with cores similarly rich in cassiterite inclusions from the Haobugao Fe–Zn polymetallic skarn deposit (Great Xing'an Range, China; Wang et al., 2018). At Haobugao, cassiterite was considered to have formed via exsolution from the late magnetite, whereas an earlier, high temperature, Sn-poor magnetite without μm-scale cassiterite inclusions was interpreted to contain this element in solid solution based on various geochemical trends. Such Sn-enrichment in magnetite is however interpreted by Wang et al. (2018) in the context of a calcic skarn, with different generations of magnetite, and thus distinct to those known from the Dulong skarn (Xu et al., 2021a). Formation of ~2–5 μm-sized cassiterite inclusions in skarn magnetite from the Lost River tin mine, Seward Peninsula (Alaska) was also

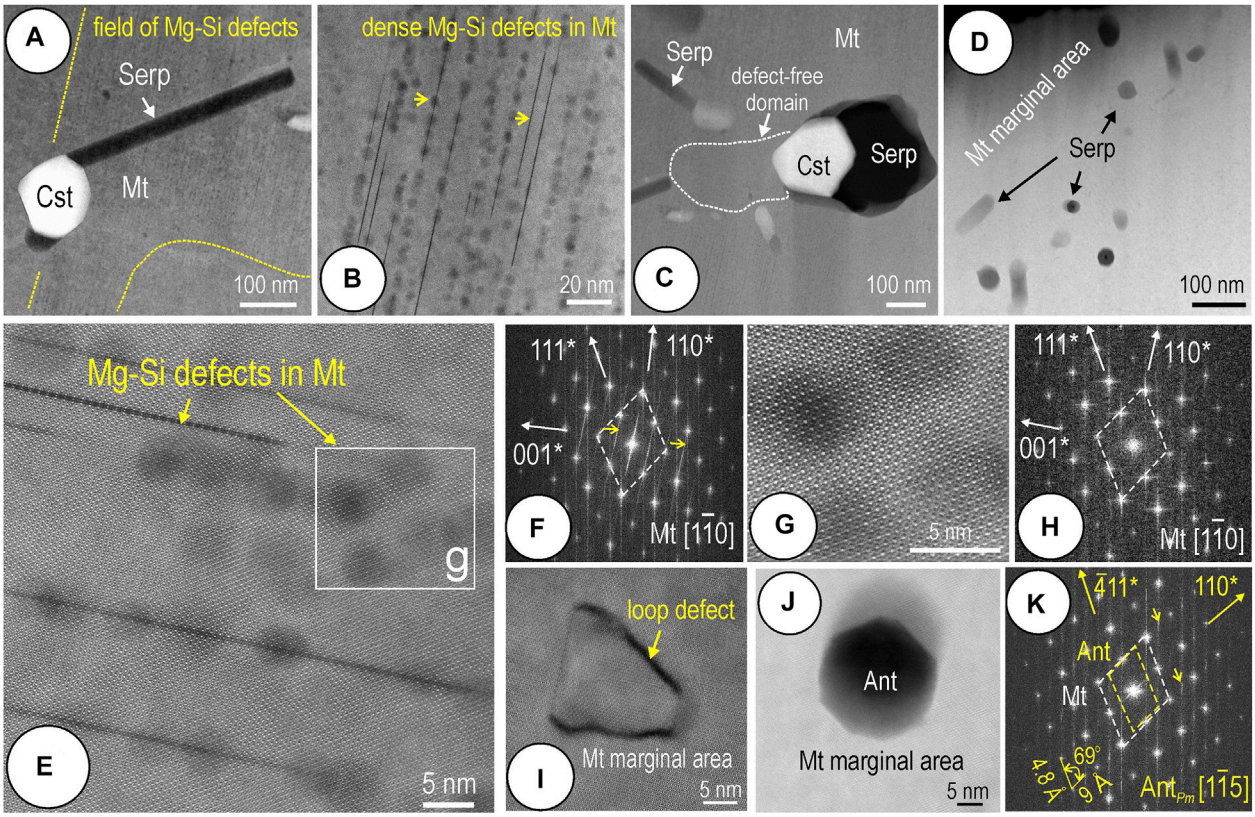

FIGURE 10
HAADF STEM images and FFT patterns for magnetite (Mt) showing defects and inclusions in the core and along the boundary to the rim. Magnetite is oriented on [1$\bar{1}$0] zone axis **(A)** Field od Mg-Si defects crosscut by serpentine (Serp) attached to cassiterite (Cst). **(B)** Dense linear Mg-Si defects showing two morphologies, thin lines, and hexagonal-shaped nanoparticles (arrowed). **(C)** Defect-free nanodomain in magnetite surrounded by inclusions of cassiterite and serpentine. **(D)** Serpentine inclusions along the boundary between the core and rim in magnetite. **(E)** High-resolution image Mg-Si defects in magnetite showing their distribution along parallel arrays. **(F)** FFT pattern for image in **(E)** showing disorder along 110* direction (yellow arrows). **(G,H)** Close-up of hexagonal defects and FFT pattern. Note that no disorder is present [compare with FFT in **(F)**]. **(I)** Loop-shaped defect in magnetite from the marginal area. FFT pattern is identical with the one shown in **(H)**. **(J,K)** Image and FFT pattern for a serpentine inclusion identified as antigorite. FFT indexing using the monoclinic *Pm* structure in Dodony et al. (2002).

attributed to exsolution from an initial solid solution based on observed epitactic/crystallographic orientations between inclusions and host oxide (Desborough and Sainsbury, 1970).

Our study shows the boundary between the core and rim in magnetite preserves evidence of multi-stage formation, rather than a single growth event. One important discovery, only revealed through a nanoscale approach, is the preservation of a Mg- and F-bearing stage (formation of sellaite and chondrodite; Figures 8, 9) since humite group minerals are key indicators of magnesium skarn predating formation of (pyroxene-garnet) calcic skarn at Dulong (Xu et al., 2021a).

This humite skarn is initiated by Mg-Si metasomatism forming fields of defects within magnetite and culminates with the discharge of volatile-rich, Sn-bearing fluids leading to formation of cassiterite inclusions within magnetite (Figures 4–6). The co-crystallization of cassiterite with serpentine from such fluids is supported by two-phase inclusions in apparent equilibrium (Figure 6B). Collectively, the defects and inclusion associations within the core are attributable to a high-temperature, prograde skarn stage. The inclusion-free rim is, however, interpreted as the result of a superimposed, retrograde stage, as evidenced from orientation of serpentine inclusions but without cassiterite underlining the scalloped contact between the magnetite core and rim (Figure 5). Retrograde stages are inherent to skarn evolution and are manifested by fluids being drawn backwards at the end of the prograde stage (Meinert, 1992; Dipple and Gerdes, 1998). Such an interpretation can explain the lack of cassiterite inclusions in the grain rims (Figures 3A,B) as Sn is dissolved by these waning fluids and reprecipitated as coarser cassiterite outside the magnetite. Likewise, a small-scale overprint is recognized from the nanodomains that are free of Mg-Si defects (Figure 10C). At this stage advanced

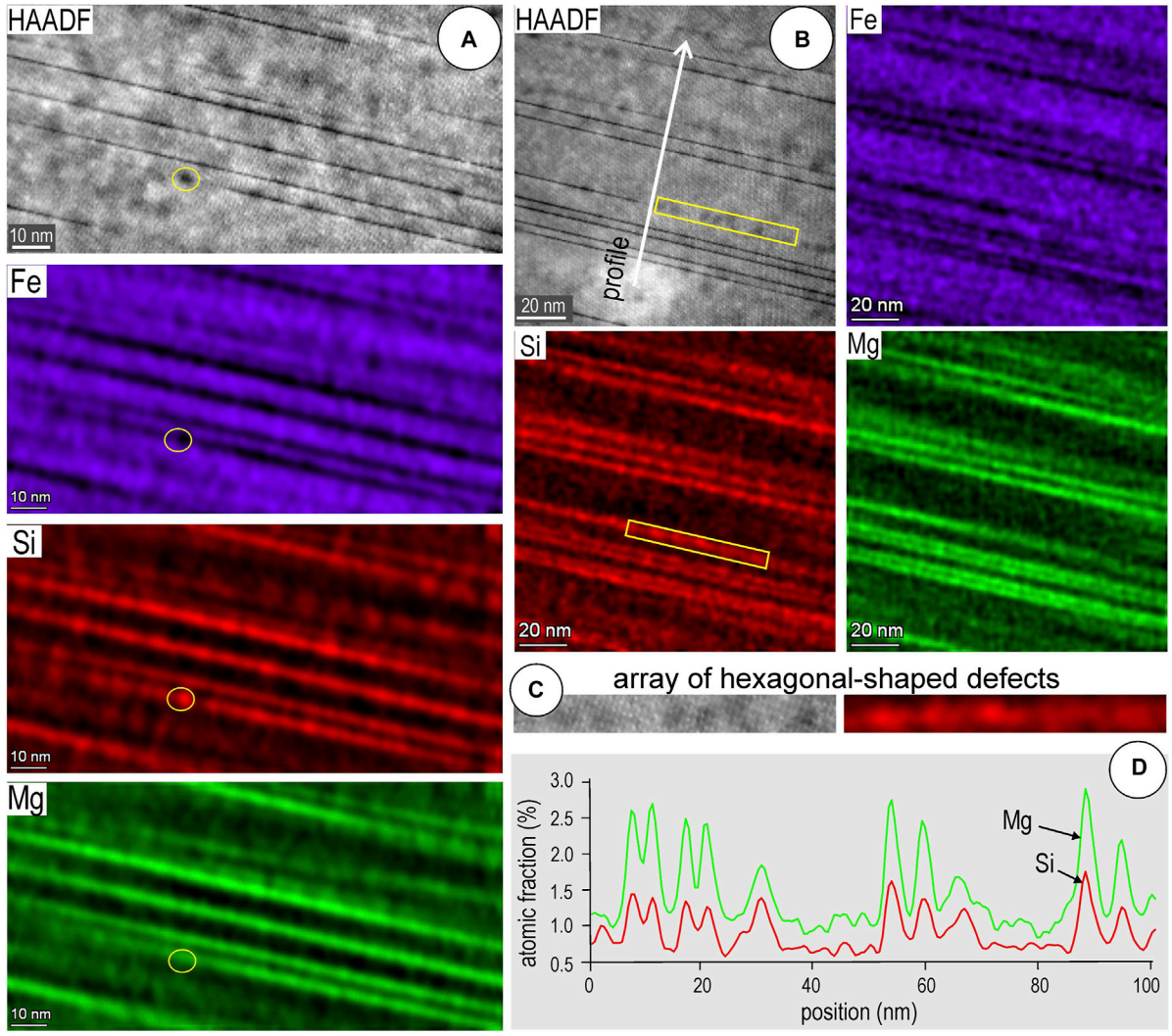

FIGURE 11
(A,B) Images and STEM EDS maps for Mg-Si defects in magnetite. Yellow circle in **(A)** highlights a single, hexagonal-shaped NP showing they are also Mg-Si-bearing. **(C)** Crop of an array of hexagonal-shaped NPs from **(B)** showing they are enriched in the same elements as the lines (Si only shown). **(D)** Profile showing the correlation between Mg and Si concentrations across the field of defects [(line marked on (b)].

serpentinization of the humite skarn is likely to occur as volatile extraction always enhances the fluid flux (e.g., Dipple and Gerdes, 1998).

5.2 Exsolutions from solid solution: Mg-Si defects predating Sn-enrichment in magnetite

The change in crystallographic directions, from defects along <110*> to epitaxial inclusion nucleation along <111*> (Figures 7A,C; 10e, f) indicates the structural control during magnetite growth and interaction with inbound fluids.

Rare spinel phases such as ringwoodite ($SiMg_2O_4$) and ahrensite ($SiFe_2O_4$), which have proven useful in petrological studies of the Earth's mantle, are considered high pressure polymorphs of minerals from the olivine group formed in the transitional zone at depths of 400–650 km (Biagioni and Pasero, 2014, and references therein). Such scenarios are clearly unrealistic to explain the formation of the Mg-Si defects shown here (Figures 11, 12). These could be attributed to diffusion-assisted exsolution processes, thus accounting for the spotted appearance (i.e., arrays of hexagonal-shaped Mg-Si-NPs) followed by fluid infiltration along (110) planes acting as twin dislocations in magnetite. They are likely to be more common than presently known in skarn magnetite.

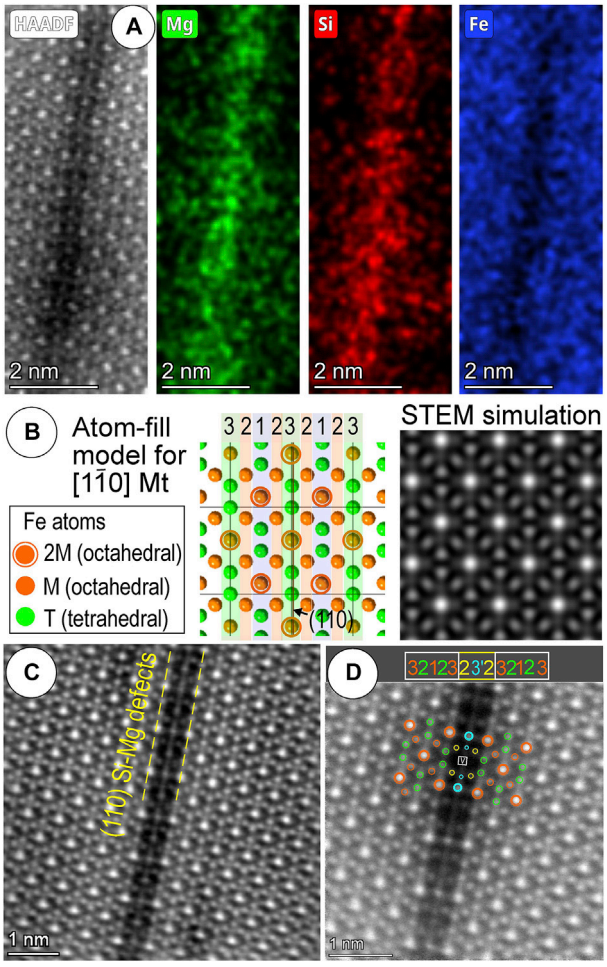

FIGURE 12
(A) High-resolution HAADF STEM and STEM EDS maps of single line defect in magnetite. Note antipathetic relationship between Si/Mg and Fe. **(B)** Atom-fill crystal structure model for Fe atoms in $[1\bar{1}0]_{magnetite}$ with sequence of octahedral (M) and tetrahedral (T) sites used for interpretation of HAADF STEM images. STEM simulation of magnetite showing the larger atoms in 2 M sites surrounded by smaller/darker dots representing M and T sites. See main text for further information. **(C,D)** Atomic scale images of a single line-defect of width ~6 Å corresponding to $2d_{110}$ in magnetite along (110) planes showing changes in HAADF intensity. Overlays in **(D)** show interpretation in terms of partial to total replacement of Fe by Mg and Si. Atomic arrangement across the defect in terms of the sequence: 3/2123/23′2/3212/3, whereby 3′ is a 3-type array with ½ (110) gaps in 2 M atoms (v represents vacancies?).

An approach like that considered for the γ-$Fe_{1.5}SiO_4$ phase observed in silician magnetite with vacancies ordered as $[v_{0.5}Fe^{2+}{}_{0.5}]^{oct}[Fe^{3+}]^{oct}Si^{tet}O_4$ (Xu et al., 2014) could be more appropriate for future studies. Indeed, Sn is among the tetravalent elements doped into magnetite, $Me_xFe_{3-x}O_4$, where Me is Ti, Sn, and Si), and $0<x<0.4$ (Hernández-Gómez et al., 2006). In the titanomagnetite system, Sn incorporation is promoted at higher temperatures via vacancy-mediated long-range substitution of Sn ions within boundaries between magnetic domains, albeit with Sn^{4+}-Fe^{2+} pairs showing lower rates of diffusion than Ti^{4+}-Fe^{2+} pairs in magnetite (Hernández-Gómez et al., 2001, 2006). An example of cassiterite particles attached to ilmenite lamellae has been shown for magmatic titanomagnetite (Wang et al., 2012).

The present study shows no unequivocal evidence for cassiterite formation from exsolution processes, despite the preferential orientation between cassiterite and serpentine inclusions along <111*> directions in host magnetite. Such orientations are rather controlled by crystal structural parameters matching each other along these directions in magnetite (Figures 7A,C, 10J,K).

5.3 Inclusions in magnetite: A record of evolving fluids and other petrogenetic implications

Studies of melt inclusions in quartz and fluid inclusions in quartz and cassiterite from topaz-albite granite from Zinnwald (Germany) have shown that F-rich hydrous melt fractions and hydrothermal fluids can form during differentiation of highly evolved Sn-granite magmas (Thomas et al., 2005). This demonstrates that F is extremely efficient in extraction and transport of Sn *via* hydrothermal fluids formed from a F-H_2O rich granitic magma, even if the Laojunshan granite is recognized as a highly fractionated, metaluminous S-type granite (Xu et al., 2015).

Such an interpretation is consistent with the presence of grossular and vesuvianite in skarns at Dulong (Xu et al., 2021a), typical of reduced assemblages in Sn-W skarn deposits (Bowman, 1998) affiliated to S-type granites (Meinert, 1997). This implies that the initial fluids, although F-rich, are not the main contributor to Sn mineralization. Magnetite within marble or calcic skarn is not a major host for Sn (Figure 2). Cassiterite from the calcic skarn and marble (Xu et al., 2021a) is thus considered to represent a later, geochemically distinct generation from the cassiterite occurring as inclusions in magnetite.

The structure and composition of magnetite is adept at preserving evidence of inherited protoliths, stages of alteration, and superimposed events, information that is critical for genetic interpretation in terranes with intensively altered lithologies. Expanding on the information obtained from traditional micron-scale techniques, an extraordinary level of detail can be accessed using HAADF STEM imaging (Xu et al., 2014; Ciobanu et al., 2019, 2022; Huang and Beaudoin, 2021; Verdugo-Ihl et al., 2021), a technique that provides a more direct visualization of atoms in the crystal structures than traditional TEM methods.

6 Conclusion and implications

In summary, the magnetite studied here preserves a range of textures that reveal initiation of the skarn system as a humite,

magnesium skarn stage (chondrodite). Magnesium-Si defects form along (110) planes prior to Sn-enrichment. The release of high-volatile, F-rich fluids can lead to precipitation of cassiterite inclusions along <111*> directions in magnetite. This is an alternative mechanism to "exsolution from solid solution" showing epitaxial growth between cassiterite and host magnetite.

In its entirety, the magnetite records the history of metasomatism during prograde core growth and retrograde rim replacement. The Dulong magnetite is the first case in which (110) Mg-Si defects are documented. This is likely to be a common feature of many skarn systems since these include Mg-bearing (calc)silicates. Such characteristics can be useful to fingerprint initiation of metasomatic processes at the atomic-scale, particularly important during changes in redox conditions at the switch between prograde and retrograde skarn regimes which also show enrichment in elements such as W and Mo, commonly associated with Sn. Magnetite that coexists with such regime changes, e.g., from more oxidizing diopside + andradite to reducing hedenbergite + grossular assemblages in calcic skarn, may record comparable complex defects and inclusion associations.

Data availability statement

The raw data supporting the conclusions of this article will be made available by the authors, without undue reservation.

Author contributions

JX and CC conceptualized this work with advice and guidance from NC and KE. FIB-SEM work was undertaken by JX and LC-D, EPMA analysis by JX and BW. STEM analysis and interpretation was performed by CC, AS and JX. The manuscript was written and revised by JX, CC and NC with contributions to figure preparation and editing of the manuscript by all other authors.

Funding

This research was funded by Scientific Funds of Fuzhou University, the National Natural Science Foundation of China (42072094), and Key Laboratory of Mineral Resources (KLMR 2017-13). Additional support was made available from the project "Trace elements in Fe-oxides: deportment, distribution and application in ore genesis, geochronology, exploration and mineral processing," supported by BHP Olympic Dam and the South Australian Government Mining and Petroleum Services Centre of Excellence.

Acknowledgments

The authors acknowledge the staff of Adelaide Microscopy (University of Adelaide) for assistance and encouragement. JX thanks Max Verdugo-Ihl for valuable discussion. Microscopy Australia were thanked for access to FEI Titan Themis instrumentation. We appreciate the comments of two reviewers and manuscript handling by Associate Editor Antoni Camprubi.

Conflict of interest

Author KE is an employee of BHP Olympic Dam.

The remaining authors declare that the research was conducted in the absence of any commercial or financial relationships that could be construed as a potential conflict of interest.

Publisher's note

References

Barkov, A. Y., Martin, R. F., Shi, L., LeBarge, W., and Fedortchouk, Y. (2008). Oscillatory zoning in stanniferous hematite and associated W- and Bi-rich minerals from Canadian Creek, Yukon, Canada. *Can. Mineralogist* 46, 59–72. doi:10.3749/canmin.46.1.59

Biagioni, C., and Pasero, M. (2014). The systematics of the spinel-type minerals: An overview. *Am. Mineral.* 99, 1254–1264. doi:10.2138/am.2014.4816

Bowman, J. R. (1998). "Basic aspects and applications of phase equilibria in the analysis of metasomatic Ca-Mg-Al-Fe-Si skarns," in *Mineralised intrusion-related skarn systems. Mineral. Assoc. Canada short course*. Editor D. R. Lentz (United Kingdom: Mineralogical Association of Canada), 26, 1–49.

Capitani, G., and Mellini, M. (2004). The modulated crystal structure of antigorite: The *m* = 17 polysome. *Am. Mineral.* 89, 147–158. doi:10.2138/am-2004-0117

Chen, J., Halls, C., and Stanley, C. J. (1992). Tin-bearing skarns of South China: Geological setting and mineralogy. *Ore Geol. Rev.* 7, 225–248. doi:10.1016/0169-1368(92)90006-7

Ciobanu, C. L., Cook, N. J., Maunders, C., Wade, B. P., and Ehrig, K. (2016). Focused ion beam and advanced electron microscopy for minerals: Insights and outlook from bismuth sulphosalts. *Minerals* 6, 112. doi:10.3390/min6040112

Ciobanu, C. L., and Cook, N. J. (2004). Skarn textures and a case study: The Ocna de Fier-Dognecea orefield, Banat, Romania. *Ore Geol. Rev.* 24, 315–370. doi:10.1016/j.oregeorev.2003.04.002

Ciobanu, C. L., Verdugo-Ihl, M. R., Cook, N. J., Ehrig, K., Slattery, A., and Courtney-Davies, L. (2022). Ferro-tschermakite with polysomatic chain-width disorder identified in silician magnetite from Wirrda Well, South Australia: A HAADF STEM study. *Am. Mineral.* 107, 765–777. doi:10.2138/am-2022-7975

Ciobanu, C. L., Verdugo-Ihl, M. R., Slattery, A., Cook, N. J., Ehrig, K., Courtney-Davies, L., et al. (2019). Silician magnetite: Si–Fe-Nanoprecipitates and other mineral inclusions in magnetite from the Olympic Dam deposit, South Australia. *Minerals* 9, 311. doi:10.3390/min9050311

Cioflica, G., Vlad, S., and Stoici, S. (1971). Repartition de la mineralisation dans les skarns de Baita Bihorului. *Rev. Roum. Geol. Geophys. Geogr. Ser. Geol.* 15, 43

Cioflica, G., Vlad, S., Volanschi, E., and Stoici, S. (1977). Magnesian skarns and associated mineralization at Baita Bihor (in Romanian). *St. Cerc. Geol. Geofiz. Geogr. Ser. Geol.* 22, 39

Cook, N. J., Ciobanu, C. L., Ehrig, K., Slattery, A. D., and Gilbert, S. E. (2022b) Micron- to atomic-scale investigation of rare earth elements in iron oxides. *Front. Earth Sci.*

Cook, N. J., Ciobanu, C. L., Ehrig, K., Slattery, A., Verdugo-Ihl, M. R., Courtney-Davies, L., et al. (2017). Advances and opportunities in ore mineralogy. *Minerals* 7, 233. doi:10.3390/min7120233

Cook, N. J., and Ciobanu, C. L. (2001). Paragenesis of Cu-Fe ores from Ocna de Fier-Dognecea (Romania), typifying fluid plume mineralization in a proximal skarn setting. *Mineral. Mag.* 65, 351–372. doi:10.1180/002646101300119457

Cook, N. J., Ciobanu, C. L., Verdugo-Ihl, M. R., Courtney-Davies, L., Ehrig, K., Li, W., et al. (2022a). Trace elements in minerals: Where do we stand on the road between the holy grail and a can of worms?" in Proc. 16th SGA Biennial Meeting, 1, 65–68.

Deditius, A. P., Reich, M., Simon, A. C., Suvorova, A., Saunders, M., Roberts, M. P., et al. (2018). Nanogeochemistry of hydrothermal magnetite. *Contrib. Mineral. Pet.* 173, 46. doi:10.1007/s00410-018-1474-1

Desborough, G. A., and Sainsbury, C. L. (1970). Cassiterite as an exsolution product in magnetite, Lost River tin mine, Alaska. *Econ. Geol.* 65, 1004–1006. doi:10.2113/gsecongeo.65.8.1004

Dipple, G. M., and Gerdes, M. L. (1998). "Reaction-infiltration feedback and hydrodynamics at the skarn front," in *Mineralized intrusion-related skarn systems. Mineral. Assoc. Canada short course*. Editor D. R. Lentz (United Kingdom: Mineralogical Association of Canada), 26, 71–97.

Dodony, I., Posfai, M., and Buseck, P. R. (2002). Revised structure models for antigorite: An HRTEM study. *Am. Mineral.* 87, 1443–1457. doi:10.2138/am-2002-1022

Einaudi, L. D., Meinert, L. D., and Newberry, R. J. (1981). "Skarn deposits," in *Seventy-Fifth Anniversary Volume*. Society of Economic Geologists, 317–391.

Friedrich, A., Lager, G. A., Kunz, M., Chakoumakos, B. C., Smyth, J. R., and Schultz, A. J. (2001). Temperature-dependent single-crystal neutron diffraction study of natural chondrodite and clinohumites. *Am. Mineral.* 86, 981–989. doi:10.2138/am-2001-8-904

Gibbs, G. V., Ribbe, P. H., and Anderson, C. P. (1970). The crystal structures of the humite minerals. II. Chondrodite. *Am. Mineral.* 55, 1182

Gower, S. J., Clark, A. H., and Hodgson, C. J. (1985). Tungsten–molybdenum skarn and stockwork mineralization, Mount Reed – Mount Haskin district, northern British Columbia, Canada. *Can. J. Earth Sci.* 22, 728–747. doi:10.1139/e85-078

Hernández-Gómez, P., Bendimya, K., De Francisco, C., Muñoz, J. M., Alejos, O., and Torres, C. (2001). Magnetic disaccommodation in Sn substituted magnetite. *J. Magn. Magn. Mat.* 226, 1409–1411. doi:10.1016/S0304-8853(00)00963-X

Hernández-Gómez, P., Bendimya, K., De Francisco, C., Torres, C., Muñoz, J. M., Alejos, O., et al. (2006). Effect of tetravalent substitutions on the magnetic disaccommodation in magnetite. *Phys. Status Solidi* 3, 3180–3183. doi:10.1002/pssc.200567051

Houzar, S., Litochleb, J., Sejkora, J., Cempírek, J., and Cícha, J. (2008). Unusual mineralization with niobian titanite and Bi-tellurides in scheelite skarn from Kamenne doly Quarry near Pisek, Moldanubian Zone, Bohemian Massif. *J. Geosci.* 53, 1–16. doi:10.3190/jgeosci.017

Huang, X. D., Lu, J. J., Zhang, R. Q., Sizaret, S., Ma, D. S., Wang, R. C., et al. (2022). Garnet and scheelite chemistry of the Weijia tungsten deposit, South China: Implications for fluid evolution and W skarn mineralization in F-rich ore system. *Ore Geol. Rev.* 142, 104729. doi:10.1016/j.oregeorev.2022.104729

Huang, X. W., and Beaudoin, G. (2021). Nanoinclusions in zoned magnetite from the Sossego IOCG deposit, Carajás, Brazil: Implication for mineral zoning and magnetite origin discrimination. *Ore Geol. Rev.* 139, 104453. doi:10.1016/j.oregeorev.2021.104453

Huberty, J. M., Konish, H., Heck, P. R., Fournelle, J. H., Valley, J. W., and Xu, H. (2012). Silician magnetite from the Dales Gorge member of the Brockman iron formation, Hamersley group, Western Australia. *Am. Mineral.* 97, 26–37. doi:10.2138/AM.2012.3864

Kontonikas Charos, A., Ehrig, K., Cook, N. J., and Ciobanu, C. L. (2019). Crystal chemistry of titanite from the Roxby Downs granite South Australia: Insights into petrogenesis subsolidus evolution and hydrothermal alteration. *Contrib. Mineral. Pet.* 174, 59. doi:10.1007/s00410-019-1594-2

Lazić, I., Bosch, E. G. T., and Lazar, S. (2016). Phase contrast STEM for thin samples: Integrated differential phase contrast. *Ultramicroscopy* 160, 265–280. doi:10.1016/j.ultramic.2015.10.011

Li, P. Y., Yan, Y. F., Yang, G. S., Jia, F. J., Tian, Z. D., Cui, D. H., et al. (2018). Mineralogical characteristics of skarns from Dulong Sn-Zn polymetallic deposit in Yunnan province and their geological significances. *Acta Min. Sin.* 38, 290–302. doi:10.16461/j.cnki.1000-4734.2018.032

Liu, Y. P., Li, Z., Li, H., Guo, L., Xu, W., Ye, F., et al. (2007). U–Pb geochronology of cassiterite and zircon from the Dulong deposit: Evidence for Cretaceous large-scale granitic magmatism and mineralization events in southeastern Yunnan Province, China. *Acta Pet. Sin.* 23, 967–976. doi:10.1631/jzus.2007.B0900

Mao, M., Rukhlov, A. S., Rowins, S. M., Spence, J., and Coogan, L. A. (2016). Apatite trace element compositions: A robust new tool for mineral exploration. *Econ. Geol.* 111, 1187–1222. doi:10.2113/econgeo.111.5.1187

Marincea, Ş., and Dumitraş, D.-G. (2019). Contrasting types of boron-bearing deposits in magnesian skarns from Romania. *Ore Geol. Rev.* 112, 102952. doi:10.1016/j.oregeorev.2019.102952

Mei, W., Lv, X. B., Cao, X. F., Liu, Z., Zhao, Y., Ai, Z. L., et al. (2014). Ore Genesis and hydrothermal evolution of the Huanggang skarn iron–tin polymetallic deposit, southern Great Xing'an Range: Evidence from fluid inclusions and isotope analyses. *Ore Geol. Rev.* 64, 239–252. doi:10.1016/j.oregeorev.2014.07.015

Meinert, L. D. (1997). Application of skarn deposit zonation models to mineral exploration. *Explor. Min. Geol.* 6, 185

Meinert, L. D., Dipple, G. M., and Nicolescu, S. (2005). "World skarn deposits," in *100th Anniversary Volume*. Society of Economic Geologists, 299–336. doi:10.5382/AV100.11

Meinert, L. D. (1992). Skarns and skarn deposits. *Geosci. Can. Repr. Ser.* 6, 117–134. doi:10.12789/gs.v19i4.3773

Nadoll, P., Angerer, T., Mauk, J. L., French, D., and Walshe, J. (2014). The chemistry of hydrothermal magnetite: A review. *Ore Geol. Rev.* 61, 1–32. doi:10.1016/j.oregeorev.2013.12.013

Neumann, E. R., Svensen, H. H., Polozov, A. G., and Hammer, Ø. (2017). Formation of Si-Al-Mg-Ca-rich zoned magnetite in an end-Permian phreatomagmatic pipe in the Tunguska Basin, East Siberia. *Min. Depos.* 52, 1205–1222. doi:10.1007/s00126-017-0717-9

Ohtaka, O., Tobe, H., and Yamanaka, T. (1997). Phase equilibria for the Fe_2SiO_4-Fe_3O_4 system under high pressure. *Phys. Chem. Min.* 24, 555–560. doi:10.1007/s002690050072

Ottolini, L., Cámara, F., and Bigi, S. (2000). An investigation of matrix effects in the analysis of fluorine in humite-group minerals by EMPA, SIMS, and SREF. *Am. Mineral.* 85, 89–102. doi:10.2138/am-2000-0110

Shiga, Y. (1988). Silician magnetite from the Kamaishi Mine. *Jpn. Min. Geol.* 38, 437–440. doi:10.11456/SHIGENCHISHITSU1951.38.437

Thomas, R., Förster, H.-J., Rickers, K., and Webster, J. D. (2005). formation of extremely F-rich hydrous melt fractions and hydrothermal fluids during differentiation of highly evolved tin-granite magmas: A melt/fluid-inclusion study. *Contrib. Mineral. Pet.* 148, 582–601. doi:10.1007/s00410-004-0624-9

Verdugo-Ihl, M. R., Ciobanu, C. L., Cook, N. J., Ehrig, K., and Courtney-Davies, L. (2020). Defining early stages of IOCG systems: Evidence from iron-oxides in the outer shell of the Olympic Dam deposit, South Australia. *Min. Depos.* 55, 429–452. doi:10.1007/s00126-019-00896-2

Verdugo-Ihl, M. R., Ciobanu, C. L., Cook, N. J., Ehrig, K., Slattery, A., Courtney-Davies, L., et al. (2021). Nanomineralogy of hydrothermal magnetite from Acropolis, South Australia: Genetic implications for iron-oxide copper gold mineralization. *Am. Mineral.* 106, 1273–1293. doi:10.2138/am-2021-7557

Wang, R. C., Yu, A. P., Chen, J., Xie, L., Lu, J. J., and Zhu, J. C. (2012). Cassiterite exsolution with ilmenite lamellae in magnetite from the Huashan metaluminous tin granite in southern China. *Mineral. Pet.* 105, 71–84. doi:10.1007/s00710-012-0194-x

Wang, X. D., Wei, W., Lv, X. B., Fan, X. J., Wang, S. B., and Liu, Y. (2018). Stanniferous magnetite composition from the Haobugao skarn Fe-Zn deposit, southern Great Xing'an Range: Implication for mineral depositional mechanism. *Geol. J.* 53, 1823–1839. doi:10.1002/gj.3009

Xu, B., Jiang, S. Y., Wang, R., Ma, L., Zhao, K. D., and Yan, X. (2015). Late cretaceous granites from the giant Dulong Sn-polymetallic ore district in Yunnan Province, South China: geochronology, geochemistry, mineral chemistry and Nd–Hf isotopic compositions. *Lithos* 218, 54–72. doi:10.1016/j.lithos.2015.01.004

Xu, H., Shen, Z., and Konishi, H. (2014). Si-Magnetite nano-precipitates in silician magnetite from banded iron formation: Z-Contrast imaging and *ab initio* study. *Am. Mineral.* 99, 2196–2202. doi:10.2138/am-2014-4964

Xu, J., Ciobanu, C. L., Cook, N. J., and Slattery, A. (2019). Crystals from the powellite-scheelite series at the nanoscale: A case study from the Zhibula Cu skarn, Gangdese belt, Tibet. *Minerals* 9, 340. doi:10.3390/min9060340

Xu, J., Ciobanu, C. L., Cook, N. J., Slattery, A., Li, X. F., and Kontonikas-Charos, A. (2021b). Phase relationships in the system ZnS-$CuInS_2$: Insights from nanoscale study of indium-bearing sphalerite. *Am. Mineral.* 106, 192–205. doi:10.2138/am-2020-7488

Xu, J., Ciobanu, C. L., Cook, N. J., Zheng, Y.-Y., Sun, X., and Wade, B. P. (2016). Skarn formation and trace elements in garnet and associated minerals from Zhibula copper deposit, Gangdese Belt, southern Tibet. *Lithos* 262, 213–231. doi:10.1016/j.lithos.2016.07.010

Xu, J., Cook, N. J., Ciobanu, C. L., Li, X. F., Kontonikas-Charos, A., Gilbert, S., et al. (2021a). Indium distribution in sphalerite from sulfide-oxide-silicate skarn assemblages: A case study of the Dulong Zn-Sn-in deposit, southwest China. *Min. Depos.* 56, 307–324. doi:10.1007/s00126-020-00972-y

Yao, Y., Chen, J., Lu, J., Wang, R., and Zhang, R. (2014). Geology and Genesis of the hehuaping magnesian skarn-type cassiterite-sulfide deposit, Hunan province, southern China. *Ore Geol. Rev.* 58, 163–184. doi:10.1016/j.oregeorev.2013.10.012

Ye, L., Bao, T., Liu, Y. P., He, F. F., Wang, X. J., Zhang, Q., et al. (2018). The trace and rare Earth elements in scheelites and their implication for the mineralization in Dulong Sn-Zn polymetal ore deposit, Yunnan Province. *J. Nanjing Uni. Nat. Sci.* 54, 245–258. doi:10.13232/j.cnki.jnju.2018.02.003

Yin, S., Wirth, R., Ma, C., and Xu, J. (2019). The role of mineral nanoparticles at a fluid-magnetite interface: Implications for trace-element uptake in hydrothermal systems. *Am. Mineral.* 104, 1180–1188. doi:10.2138/am-2019-6996

Zhao, Y., Zhang, Y., and Bi, C. (1999). Geology of gold-bearing skarn deposits in the middle and lower Yangtze River Valley and adjacent regions. *Ore Geol. Rev.* 14, 227–249. doi:10.1016/S0169-1368(99)00008-6

Zhao, Z., Hou, L., Ding, J., Zhang, Q., and Wu, S. (2018). A genetic link between Late Cretaceous granitic magmatism and Sn mineralization in the southwestern South China Block: A case study of the Dulong Sn-dominant polymetallic deposit. *Ore Geol. Rev.* 93, 268–289. doi:10.1016/j.oregeorev.2017.12.020